

Tuning OH binding energy enables selective electrochemical oxidation of ethylene to ethylene glycol

Yanwei Lum^{1,4}, Jianan Erick Huang^{1,4}, Ziyun Wang¹, Mingchuan Luo¹, Dae-Hyun Nam¹, Wan Ru Leow¹, Bin Chen¹, Joshua Wicks¹, Yuguang C. Li¹, Yuhang Wang¹, Cao-Thang Dinh¹, Jun Li^{1,2}, Tao-Tao Zhuang¹, Fengwang Li¹, Tsun-Kong Sham³, David Sinton² and Edward H. Sargent^{1*}

There is significant interest in developing efficient electrochemical processes for commodity chemical manufacturing, all directly powered by renewable electricity. A vital chemical is ethylene glycol, with an annual consumption of around 20 million tonnes due to its use as antifreeze and as a polymer precursor. Here we report a one-step electrochemical route at ambient temperature and pressure in aqueous media to the selective partial oxidation of ethylene to ethylene glycol. Tuning of the catalyst OH binding energy was hypothesized to be crucial for facilitating the transfer of OH to ^{*}C₂H₄OH to form ethylene glycol. Computational studies suggested that a gold-doped palladium catalyst could perform this step efficiently, and experimentally we found it to exhibit an approximate 80% Faradaic efficiency to ethylene glycol, retaining its performance for 100 hours of continuous operation. These findings represent a significant advance in the development of selective anodic partial oxidation reactions in aqueous media under mild conditions.

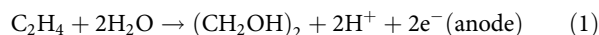
The manufacture of commodity chemicals consumes a vast amount of energy: in the United States, for instance, chemical manufacturing constitutes ~20% of the total energy consumed by the industrial sector¹. Commodity chemicals such as glycols, ammonia and organic acids are used, for example, in the manufacture of polymers, fertilizer, coatings and adhesives. Today, the energy needed for these processes is met through the consumption of fossil fuels, and thus these processes both deplete a finite resource and also contribute to CO₂ emissions into the environment^{2–6}.

One strategy to tackle these problems is to develop electrochemical processes to manufacture these commodity chemicals by the direct utilization of increasingly available renewable electricity, preferably under conditions of ambient temperature and pressure^{7–11}. Electrification of the chemicals industry could also decentralize the production of chemicals, allowing chemical valorization to occur nearer the supply of inputs (input chemicals and renewable electricity), reducing the associated processing and transportation costs⁸. Electrochemistry also directly utilizes electrons as reagents, negating the need for the use of stoichiometric amounts of potentially toxic oxidizing or reducing agents¹², which are at present heavily employed in the chemicals industry.

We identified ethylene glycol as an interesting candidate to demonstrate an electrochemical synthesis route in light of its importance as a precursor in the manufacture of polymers and its use in antifreeze. These and other applications generate an annual demand for ethylene glycol of around 20 million tonnes (ref. ¹³).

Today, the production of ethylene glycol from ethylene is a two-step process, via the intermediate oxirane¹⁴, generating about 1.6 tonnes of CO₂ per tonne of ethylene glycol produced¹⁵ (Fig. 1a).

Electrochemistry could potentially offer a direct one-step route from ethylene that could avoid cost-adding steps associated with the processing and purification of intermediates. Also, because it is an anodic oxidation reaction, the process could be coupled with CO₂ (ref. ¹⁶) or water reduction to generate, respectively, hydrocarbons or hydrogen simultaneously. The reactions for the latter process are as follows:



The approach is depicted in Fig. 1b and a techno-economic analysis (TEA) on the plant-gate levelized cost per tonne is presented in Supplementary Note 1 (Supplementary Figs. 1 and 2), indicating the economic potential of this process.

A survey of prior literature reveals that ethylene can electrochemically be partially oxidized to a variety of products such as acetaldehyde, acetic acid and oxirane^{17–19}. Reports of ethylene glycol electroproduction are rare, with work by Holbrook and Wise in 1975 providing an example that relied on a silver working electrode²⁰ and that led to total current densities in the order of 10^{–3} mA cm^{–2} and unquantified Faradaic efficiencies to ethylene glycol.

In summary, ethylene can be oxidized in different ways; the challenge is to engineer a catalyst to steer the oxidation selectively towards ethylene glycol. The selective electrooxidation to ethylene glycol would require the successive transfer of two OH groups to ethylene, which we postulate to involve the intermediate ^{*}C₂H₄OH.

¹Department of Electrical and Computer Engineering, University of Toronto, Toronto, Ontario, Canada. ²Department of Mechanical and Industrial Engineering, University of Toronto, Toronto, Ontario, Canada. ³Department of Chemistry, University of Western Ontario, London, Ontario, Canada.

⁴These authors contributed equally: Yanwei Lum, Jianan Erick Huang *e-mail: ted.sargent@utoronto.ca

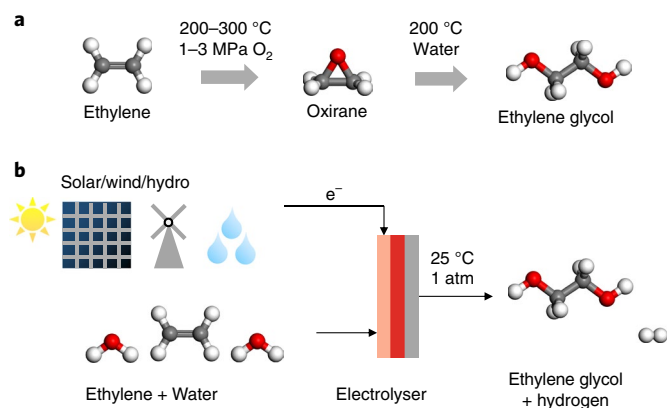


Fig. 1 | An electrochemical route to ethylene glycol. **a**, Illustration of the current industrial route. **b**, Proposed electrochemical route for the synthesis of ethylene glycol from ethylene.

We thus reasoned that the OH binding energy would be a key factor in our process. Furthermore, once ethylene glycol is formed, it likely adsorbs to the catalyst surface through its oxygen atoms: thus, tuning the OH binding energy (related to O binding energy through scaling relations²¹) could enable its facile desorption, thereby avoiding unwanted further oxidation.

Here we report that ethylene glycol is produced when ethylene is electrochemically oxidized on a palladium catalyst. Density functional theory calculations revealed that the second OH transfer, involving the *C_2H_4OH intermediate, to form ethylene glycol was the likely bottleneck. Computational screening of ten different metallic dopants in palladium identified gold as the most promising to enhance selectivity by tuning the OH binding energy. This then led us to synthesize a gold-doped palladium catalyst that exhibits ~80% selectivity for ethylene glycol and high stability: the catalyst retains its performance for 100 hours of continuous operation.

Results

Palladium nanostructured dendritic catalysts. Electrochemical deposition was used (see Methods) to construct a palladium nanostructured dendritic (Pd DNT) catalyst on a glassy carbon substrate. The resulting morphology was characterized using electron microscopy (Fig. 2a,b and Supplementary Figs. 3 and 4). Bulk electrolysis measurements were carried out using a three-electrode configuration: Ag/AgCl (3.0 M KCl) was used as the reference electrode, platinum foil as the counter electrode (cathode) and Pd DNT as the working electrode (anode). Experiments were performed for 2 hours with an ethylene-saturated aqueous 0.1 M NaClO₄ solution in an H-cell using a range of applied potentials (see Methods). We note that the electrolyte used does not have buffering capability and consequently the local pH drifts with time. The drawback in this case is that, for electrochemical reactions involving proton transfer, such as this work, the applied potential versus the RHE (reversible hydrogen electrode) changes with time and is therefore not well defined. Attempts were made to use buffered electrolytes, however, system performance in buffered electrolytes was poor (further details are given below).

At the end of the experiments, the products accumulated in the anode chamber were quantified using ¹H NMR spectroscopy. As a control, a commercial Pd/C catalyst (Fig. 2c and Supplementary Fig. 5) was tested under identical experimental conditions. The resulting ethylene glycol Faradaic efficiencies (FEs) and partial current densities for both catalysts are shown in Fig. 2d,e. The results show that Pd DNT selectively generates ethylene glycol with an FE of ~60% and a partial current density of 2.5 mA cm⁻² at 1.1 V vs Ag/AgCl. Across all the applied potentials, Pd DNT

exhibits higher ethylene glycol selectivity and partial current density compared with Pd/C.

Additionally, glycolaldehyde, acetaldehyde, oxirane and formic acid were detected as minor products (the Faradaic efficiencies are shown in Supplementary Fig. 6). Experiments involving the electrochemical oxidation of an ethylene glycol solution indicated that glycolaldehyde and formic acid form as a result of ethylene glycol oxidation (Supplementary Fig. 7). Oxirane and acetaldehyde come from a different pathway, directly from the oxidation of ethylene.

To validate our results, we performed bulk electrolysis with ¹³C-labelled ethylene (¹³CH₂¹³CH₂) under the same conditions. ¹³C NMR (Fig. 2f) and ¹H NMR (Supplementary Fig. 8) analyses indicated that the products consisted entirely of ¹³C, confirming that they are generated from the oxidation of ethylene.

Catalyst activation process. We made the following surprising observation during bulk electrolysis with Pd DNT: the total current density decreases continuously in the initial period, then starts to increase rapidly and finally levels off once a certain current density is attained (Supplementary Fig. 9). In addition, the duration of the initial period is a function of applied potential: it decreases as the applied potential becomes more positive (Supplementary Fig. 9f). By contrast, this effect is not observed with the commercial Pd/C catalyst (Supplementary Fig. 10): its current density decreases gradually over time. To elucidate further the temporal evolution of the current density and its relationship with the FE toward ethylene glycol, we performed bulk electrolysis at 1.1 V vs Ag/AgCl for 6 hours and removed aliquots of the electrolyte at various time intervals (Fig. 3a). We calculated the FE for each time interval, as shown in Fig. 3b. Both the FE and current density increase with time: in summary, Pd DNT undergoes an activation process.

We hypothesized the following explanations for this activation effect: (1) interaction of the catalyst with ethylene, (2) continuous formation of an oxide layer during electrolysis, (3) generation of Pd⁴⁺ states on the catalyst, (4) catalyst morphology/surface area effects, (5) continuous change in electrolyte pH because an unbuffered electrolyte was used or (6) continuously increasing coverage of adsorbed *OH on the catalyst surface, which occurs dynamically upon application of a potential.

To determine whether the presence of ethylene is necessary for this activation process, we performed an experiment in which the same potential was applied for 1 hour while the electrolyte was sparged with argon. After 1 hour, the argon flow was stopped and ethylene was immediately introduced into the system (Fig. 3c); the system was allowed to react for a further 3 hours. As soon as ethylene was present, the current density increased sharply and within 10 min it had reached a similar value to that achieved when ethylene had been present from the beginning. Furthermore, the FE toward ethylene glycol was calculated to be 65%, a similar value to that attained previously (Fig. 2d). We thus conclude that ethylene is not necessary for catalyst activation.

Regarding scenario (2), because an anodic potential was applied, palladium could exist in an oxidized state under our conditions. To investigate this, we carried out in situ Raman spectroscopy while applying a potential of 1.1 V vs Ag/AgCl. A broad band centred at 540 cm⁻¹ appeared upon application of the potential (Fig. 3d), and this disappeared immediately after a reducing potential was applied (Supplementary Fig. 12a). This is in contrast to the spectrum of a PdO reference sample, in which a sharp peak centred at 640 cm⁻¹ is observed (Supplementary Fig. 12b). Drawing parallels with observations by Koper and co-workers on the platinum system, we conclude that an amorphous hydrated PdO_x layer forms on the catalyst surface as result of the applied potential²². In Koper's work, the use of D₂O as the electrolyte resulted in a shift of the broad band, indicating the presence of OH groups in the oxide layer²². We too found

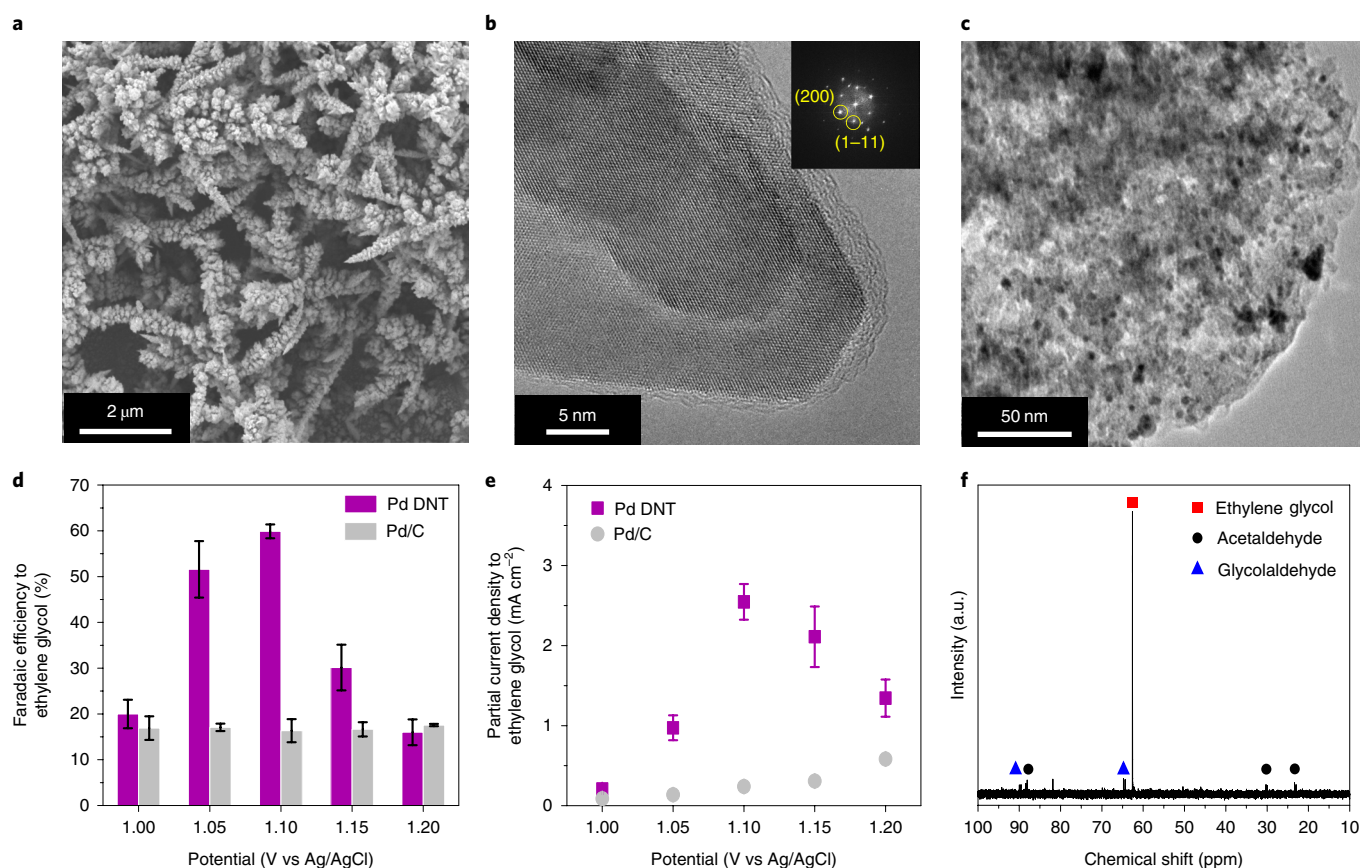


Fig. 2 | Electron microscopy characterization and ethylene oxidation using the Pd DNT and commercial Pd/C catalysts. a, SEM image of the Pd DNT catalyst. **b,** High-resolution transmission electron microscopy (TEM) image of the Pd DNT catalyst. Inset: fast Fourier transform image. **c,** TEM image of the commercial Pd/C catalyst showing Pd nanoparticles dispersed on a carbon support. **d,** FEs toward ethylene glycol formation at various applied potentials with Pd DNT and commercial Pd/C catalysts. **e,** Ethylene glycol partial current densities observed at various potentials with Pd DNT and commercial Pd/C catalysts. **f,** ^{13}C NMR spectrum of the products generated by electrochemical oxidation of ^{13}C -labelled ethylene ($^{13}\text{CH}_2^{13}\text{CH}_2$). Error bars correspond to the standard deviation of three independent measurements.

that when we switched H_2O with D_2O , the broad band shifted to 510 cm^{-1} (Fig. 3d), allowing us to conclude that OH groups are also present in our case.

To investigate scenarios (2) and (3) further, we carried out operando X-ray absorption spectroscopy (XAS). The extended X-ray fine structure (EXAFS) results confirm that the catalyst does indeed become partially oxidized (Fig. 3e). The fitting results show that $\sim 15\%$ of the catalyst becomes oxidized after 30 minutes of operation, and that this stays roughly constant even after another 30 minutes of operation (Supplementary Fig. 13). Because XAS probes the oxidation state of the bulk (due to the micrometre length penetration depth²³), we deduce this means that an oxide layer forms on the surface under the reaction conditions, and that this terminates once the entire surface is oxidized with the catalyst core remaining metallic palladium. However, if hypothesis (2) were true, we would observe the oxide grow continuously, in tandem with the catalyst activation process. As for scenario (3), the XAS spectra show no new peaks that could be attributed to Pd^{4+} , leading us to believe that this scenario is unlikely.

Once we had completed the 6 hour bulk electrolysis experiment depicted in Fig. 3a,b, we removed the electrolyte and replenished it with fresh electrolyte. Bulk electrolysis was then restarted with the same Pd DNT sample at the same potential of 1.1 V vs Ag/AgCl. From the current profile (Supplementary Fig. 15), it appears that the catalyst yet again goes through another round of activation before attaining a similar current density and Faradaic efficiency to that of

the fully activated state. However, the catalyst should already possess an oxide layer from the previous 6 hour experiment and thus these experiments do not lend support to scenarios (2) and (3).

To investigate scenario (4), we performed bulk electrolysis at 1.1 V vs Ag/AgCl for different durations (300 s, 1,500 s, 1 h and 2 h) and characterized the morphology of the catalyst by scanning electron microscopy (SEM; Supplementary Fig. 16). We saw no discernible differences. The electrochemically active surface areas (ECSAs) of Pd DNT and Pd/C were also determined by CO stripping before and after 2 hours of bulk electrolysis measurements (Supplementary Fig. 17 and Supplementary Table 1). On the basis of these results, we found that the ECSAs of the catalysts did not change significantly after bulk electrolysis. Furthermore, the ECSAs of Pd DNT and Pd/C (roughness factors of 57 and 43, respectively) are not significantly different, ruling out surface area effects as the sole cause of the higher selectivity and current density observed with Pd DNT.

To determine whether the dendritic morphology of Pd DNT was critical for catalyst activation, we tested three other palladium catalysts: a micrometre-sized powder sample (Pd powder), palladium nanoparticles (Pd NPs) and palladium oxide hydrate ($\text{PdO}\cdot\text{H}_2\text{O}$), see Supplementary Figs. 18–20 for electron microscopy, XPS and XAS characterization. Importantly, these samples have morphologies that are irregular and undefined, showing little similarity to Pd DNT. These catalysts were then tested in 2 hour bulk electrolysis experiments at 1.1 V vs Ag/AgCl. The Pd powder and Pd NPs behaved similarly, attaining a low partial current density and FE

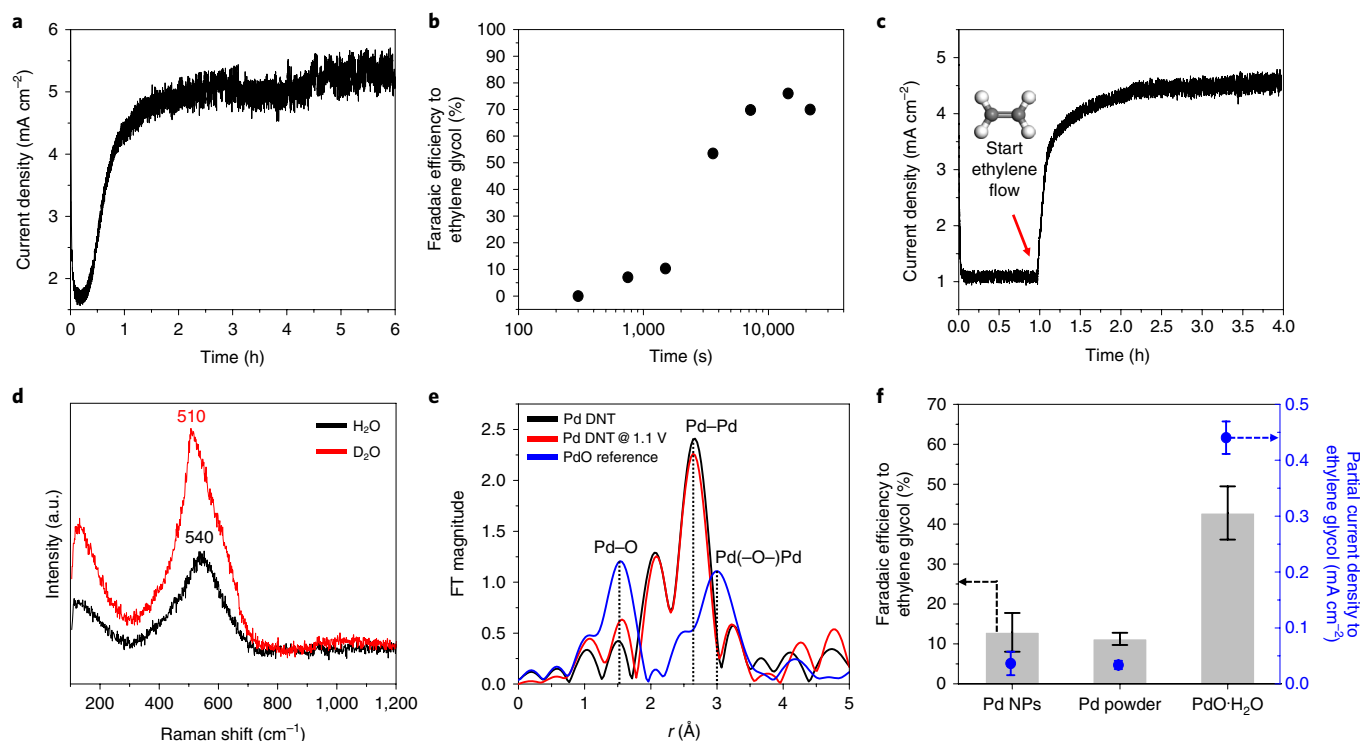


Fig. 3 | Investigation of the activation process involving the Pd DNT catalyst. **a**, Current density vs time profile for ethylene oxidation carried out for 6 h at 1.1 V vs Ag/AgCl. **b**, FEs toward ethylene glycol at various time intervals of the 6 h measurement. **c**, Current density vs time profile for the case in which ethylene was introduced into the system only after 1 h and allowed to react for a further 3 h. The FEs for all the products are shown in Supplementary Fig. 11. **d**, In situ Raman spectroscopy of Pd DNT performed at 1.1 V vs Ag/AgCl in H₂O and D₂O. **e**, EXAFS measurements of Pd DNT at a potential of 1.1 V vs Ag/AgCl. Data for Pd DNT before electrolysis and a PdO reference sample are shown as well. More detailed XAS data are shown in Supplementary Figs. 13 and 14. **f**, Faradaic efficiencies and partial current densities towards ethylene glycol for Pd NPs, Pd powder and PdO·H₂O. Error bars correspond to the standard deviation of three independent measurements.

(~10%) toward ethylene glycol (Fig. 3f) with their current densities increasing only slightly with time (Supplementary Fig. 21), indicating that these catalysts are able to undergo only minimal activation. To investigate the formation of an oxide layer, we performed in situ Raman spectroscopy on the Pd NPs (Supplementary Fig. 22). PdO·H₂O achieved a relatively high current density and FE (~44%), as shown in Fig. 3f. As in the case of Pd DNT, the current density in this case also increases significantly over time (Supplementary Fig. 21), which means that an activation effect is also observed here, even though its morphology is very different from that of Pd DNT. This rules out scenario (4) as an explanation for the activation effect. Additionally, an activation process is seen with PdO·H₂O even though it already starts as an oxide before the experiment, further ruling out scenario (2).

With regards to scenario (5), because an unbuffered electrolyte was used, it is possible that the pH changes continuously as the reaction proceeds, providing an explanation for the activation. Indeed, measuring the pH of aliquots taken at various time intervals shows that the electrolyte becomes more acidic with time, with the pH reaching 3.24 after 2 hours (Supplementary Fig. 23). However, an extensive series of experiments were carried out that showed that the pH does not control the activation process, and these results are fully detailed in Supplementary Note 2 (Supplementary Figs. 23–26). We note that two phosphate buffer systems at pH 2 and 7 were employed in these experiments, however, no activation process was observed (Supplementary Fig. 26) and the current density and FE were low, which we postulate to be due to the specific adsorption of anions.

Finally, we investigated scenario (6), in which dynamic surface reconstruction could alter the catalyst binding energy, affecting the

coverage of *OH intermediates and activating the catalyst towards ethylene glycol formation. We hypothesized that cyclic voltammetry (CV) studies could enable us to correlate catalytic activity with the presence of these adsorbed intermediates. Because catalyst activation does not require the presence of ethylene (Fig. 3c), all CV experiments were carried out in N₂-sparged 0.1 M NaClO₄ solution. Fig. 4a shows the stable CV of Pd DNT recorded at a rate of 100 mV s⁻¹. To investigate the activation process, we applied a potential of 1.1 V vs Ag/AgCl for different durations before carrying out CV. Fig. 4b shows the CV measured after the potential was held for 75 seconds and the reduction peak appears to grow larger and shift towards more cathodic regions (green arrow). Immediately after this CV cycle, a second cycle was performed without carrying another potential hold, and it was observed that the reduction peak returns to its original size and position (red arrow). When we held the potential for longer durations, we noticed that this reduction peak grew larger and shifted to more cathodic regions (Fig. 4c). Additionally, an experiment was carried out in which the potential was held for 1 hour and then the system was left at the open circuit potential for 1 minute before carrying out CV. Interestingly, with the introduction of this 1 minute pause, the reduction peak reduces in size and shifts to more anodic regions (Fig. 4d).

Taken together, these results show that the size and cathodic shift of the reduction peak is correlated to catalyst activation. This peak is likely to have multiple contributions; one source is the reduction of PdO to metallic palladium, and another we postulate to be the reduction of surface hydroxyl intermediates such as *OH. The results of these CV experiments are consistent with our observations of catalyst activation: the growth and shift of the reduction

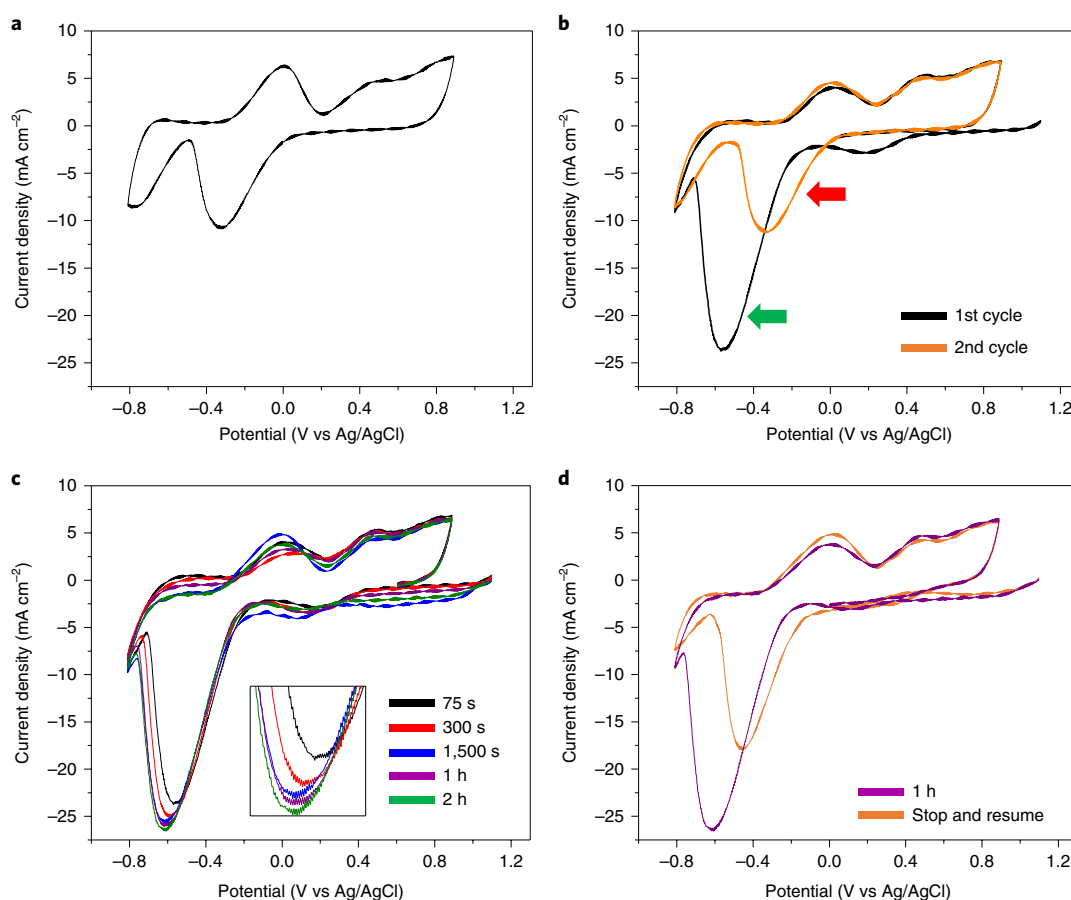


Fig. 4 | Cyclic voltammetry experiments. **a**, Stable CV of the Pd DNT catalyst in 0.1M NaClO₄ (pH 7), recorded at 100 mV s⁻¹. **b**, The potential was held at 1.1 V vs Ag/AgCl for 75 s and CV was then immediately carried out. Note that in the second cycle, a 75 s potential hold was not carried out. **c**, Similar experiments to those in **b** were carried out, but with the potential held for longer durations before carrying out CV. Inset: magnification of the reduction peak. **d**, The potential of 1.1 V vs Ag/AgCl was held for 1 h and then the system was left at the open circuit potential for 1 min before carrying out the CV (stop and resume). The CV where no pause was present is shown again here for comparison (1 h).

peak with time (Fig. 4c) mirrors the catalyst activation process, and when we conducted an experiment in which ethylene oxidation bulk electrolysis was carried out with Pd DNT for 1 hour and then left at the open circuit potential for 1 minute, the catalyst required another activation period before becoming activated again (Supplementary Fig. 27). We link this to the results shown in Fig. 4d in which the reduction peak reduces in size and shifts to anodic regions as a result of the 1 minute pause. Additional CV studies provided further evidence linking this reduction peak to catalyst activation (Supplementary Note 3, Supplementary Figs. 28 and 29).

We postulate that the increase in the reduction peak area with longer durations is due to increasing coverage of surface-adsorbed hydroxyl intermediates such as *OH, as proposed in scenario (6). This might be a result of constant dynamic catalyst surface reconstruction, which alters the OH binding energy, thus affecting its coverage. Importantly, an increased *OH coverage and altered OH binding energy likely promotes ethylene glycol formation and results in the catalyst activation that we experimentally observe. We propose that this occurs only on Pd DNT and PdO-H₂O because these catalysts may exhibit a higher degree of defects/disorder, which makes them prone to reconstruction under an applied potential.

Dopant tuning of OH binding energy. These findings motivated us to explore additional variables to tune the OH binding energy towards further improving catalyst selectivity. Modifying the OH

binding energy through dopants should modulate the FE. Using density functional theory (DFT), we explored a reaction mechanism in which lattice OH in PdO serves as a direct reaction intermediate for the formation of ethylene glycol (Fig. 5a). We carried out simulations on a PdO (100) slab (calculation details can be found in the Methods section). From these calculations, we identified the most likely limiting step to be OH addition to the *C₂H₄OH intermediate (IV → V) due to its high energy change of 0.74 eV. To lower this, we screened ten different metallic dopants, calculating the energy change for all the steps in the reaction mechanism. For all elements, we considered two possible substitutional dopant positions, on the surface and on the subsurface (Fig. 5b).

Figure 5c shows the effect of these metallic dopants on the energy change for the step IV → V (subsurface position). From these results, gold was identified as the most promising dopant, with an exergonic energy change (-0.06 eV). Furthermore, the desorption of ethylene glycol (V → VI) is more facile with gold doping (Supplementary Table 2), which is beneficial for preventing unwanted further oxidation. On the other hand, a dopant such as rhodium has the opposite effect as it increases the energy of the limiting step (Fig. 5c) and should have a negative effect on the ethylene glycol FE. These results are rationalized in terms of the OH binding energy of the dopants, with rhodium having a stronger and gold a weaker binding energy compared with palladium (ref. 24). A similar conclusion is reached for these dopants in a surface position (Supplementary Table 3).

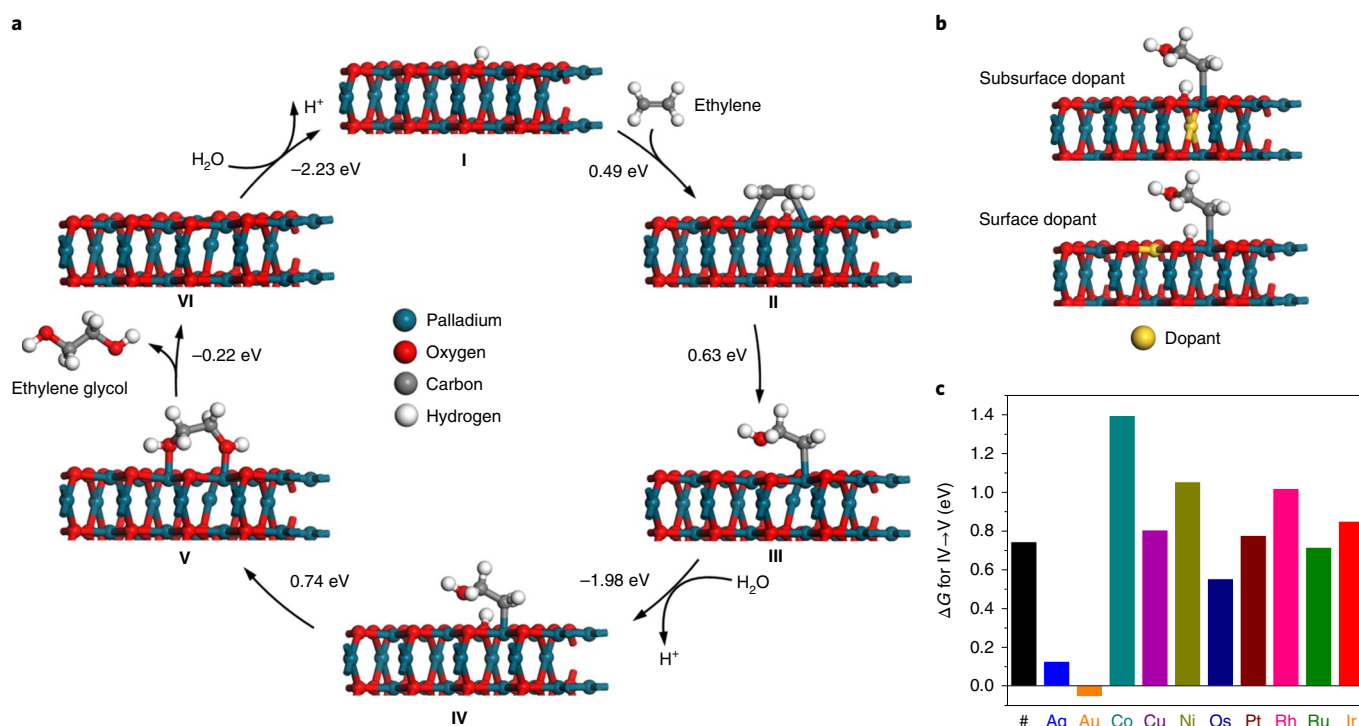


Fig. 5 | Density functional theory calculations for ethylene oxidation to ethylene glycol. **a**, Possible reaction mechanism involving lattice OH, simulated on a PdO (100) slab. Structure I: PdO + OH. Structure II: $^*C_2H_4 + OH$. Structure III: *C_2H_4OH . Structure IV: $^*C_2H_4OH + OH$. Structure V: $^*C_2H_4(OH)_2$. Structure VI: PdO with surface O vacancy. The applied potential was taken to be 1.7 V vs RHE. **b**, Illustration of the two different possible dopant positions (surface and subsurface). Structure IV is illustrated in both cases. **c**, DFT calculation results of the free energy change (ΔG) for the step IV \rightarrow V for ten different dopant elements in the subsurface dopant position. # represents the case in which no dopant is used. Each element is represented by a different colour for clarity.

Motivated by these results, we designed a series of experiments that would utilize gold doping with the goal of boosting catalyst selectivity. Catalysts with three different doping concentrations were fabricated (1.8, 3.2 and 9.0 at.%) by simply adding small amounts of $H[AuCl_4]$ to the electrodeposition solution (see Methods), and the compositions were determined using inductively coupled plasma optical emission spectrometry (ICP-OES) analysis (Supplementary Table 4). The SEM image of the catalyst with 3.2 at.% Au is shown in Fig. 6a, and the XPS spectra are given in Supplementary Fig. 30. Testing these catalysts in 2 hour bulk electrolysis experiments showed that the catalysts with 1.8 and 3.2 at.% Au did indeed enhance the FE toward ethylene glycol to 67 and 70%, respectively (Supplementary Fig. 31). However, for the catalyst with 9.0 at.% Au, the FE decreased to 54%, indicating that excessive gold doping has a negative effect, likely because the OH binding energy is no longer optimal for ethylene glycol formation. Because the 3.2 at.% Au catalyst had the highest FE, we named this catalyst PdAu DNT and investigated the effect of applied potential on the FE, as shown in Fig. 6b and Supplementary Fig. 31e. The results clearly show that gold addition boosts the FE and partial current density toward ethylene glycol, except at the higher applied potentials. As with the Pd DNT catalyst, PdAu DNT also appears to go through an activation process (Supplementary Figs. 32 and 33). A 6 hour bulk electrolysis experiment was carried out with PdAu DNT and it was also observed that the current density and FE increase with time (Fig. 6c,d). As a negative control, doping with rhodium resulted in a lower FE toward ethylene glycol (Supplementary Figs. 34 and 35), in agreement with theoretical predictions (Supplementary Tables 2 and 3).

To evaluate whether surface area effects could explain the differences in catalytic performance of PdAu DNT and Pd DNT, we obtained the ECSAs of these catalysts by CO stripping. The ECSAs

of the DNT catalysts were found to be similar (Supplementary Table 5), thus ruling out surface area effects. Powder X-ray diffraction patterns for all the PdAu catalysts were also obtained (Supplementary Fig. 36), and we observed no evidence of phase segregation. However, we found some evidence for gold segregation for the catalyst with 9.0 at.% Au, which could explain its decreased selectivity towards ethylene glycol. XAS measurements were also performed on PdAu DNT at the Au- L_3 edge and a lower peak intensity compared with gold foil in the EXAFS spectra (Supplementary Fig. 37) corresponds to less Au–Au coordination, which is consistent with the formation of a Pd–Au alloy^{25,26}. Additionally, we performed CV measurements with PdAu DNT, similar to those carried out with Pd DNT (Supplementary Note 4). Likewise, we were able to correlate catalyst activation with the growth and cathodic shift of the CV reduction peak (Supplementary Fig. 38).

Finally, we performed bulk electrolysis with the PdAu DNT catalyst for a continuous period of 100 hours, during which we routinely removed portions of the electrolyte for NMR analysis, replacing it with fresh electrolyte. This is akin to an industrial continuous manufacturing process, in which portions of the electrolyte are routinely siphoned out of the reactor for ethylene glycol extraction. During the 100 hours, an average 80% FE toward ethylene glycol at a partial current density of 5.7 mA cm⁻² was attained (Fig. 6e) with no significant loss of performance. At the end, the mass loading and composition of the catalyst were analysed using ICP-OES (Supplementary Table 4), which showed no significant loss of mass or change in composition as a result of a prolonged period of operation.

Conclusions

We have developed an electrochemical process in which ethylene is directly oxidized to ethylene glycol in aqueous media at ambient

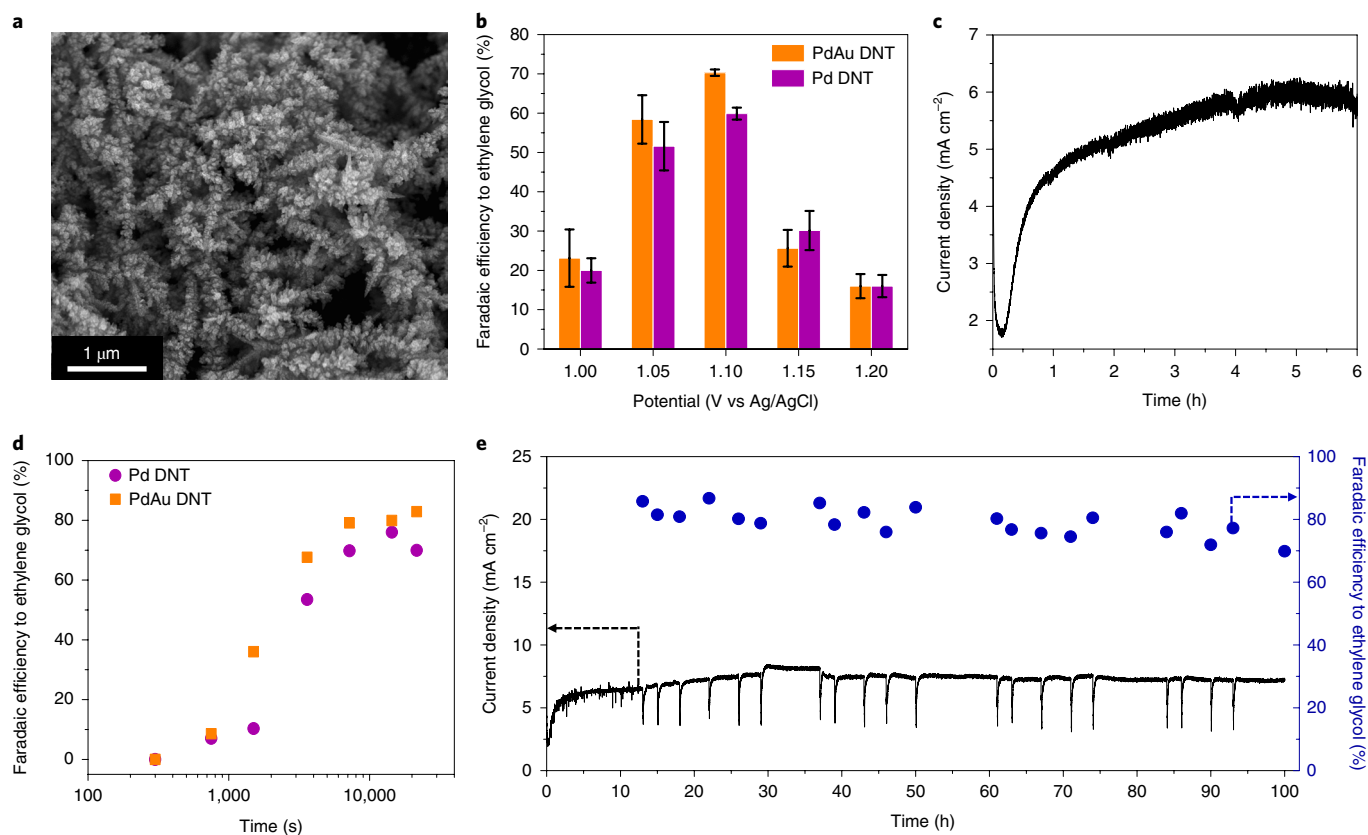


Fig. 6 | Characterization and bulk electrolysis testing of PdAu DNT catalyst. **a**, SEM image of the PdAu DNT catalyst. **b**, FEs toward ethylene glycol for PdAu DNT and Pd DNT at various applied potentials. **c**, Current density vs time profile for ethylene oxidation carried out for 6 h at 1.1 V vs Ag/AgCl. **d**, FEs toward ethylene glycol for PdAu DNT at various time intervals in the 6 hour measurement. The data for Pd DNT are also included for comparison. **e**, Continuous operation for 100 h at 1.1 V vs Ag/AgCl with PdAu DNT showing the current density profile vs time and FEs toward ethylene glycol. An average of ~80% FE and 5.7 mA cm⁻² partial current density towards ethylene glycol is maintained throughout. The FEs for other products are shown in Supplementary Fig. 39. The spikes in the current density profile occur whenever a portion of the electrolyte is removed and replenished with fresh solution. Error bars correspond to the standard deviation of three independent measurements.

temperature and pressure, a process that could potentially be powered directly by renewable electricity. This was achieved with a gold-doped palladium catalyst (3.2 at.% Au) that exhibits ~80% FE at a partial current density of 5.7 mA cm⁻², retaining its performance for 100 hours of operation at 1.1 V vs Ag/AgCl. Simultaneously, valuable hydrogen is continuously generated at the counter electrode. In addition, an activation process was observed for this catalyst; we propose that this may be related to a dynamic surface reconstruction that results in the OH binding energy of the catalyst evolving over time. Further work is needed to provide a firmer understanding of the precise nature of the activation process. The insights gained from this work provide a useful starting point for designing other anodic partial oxidation reactions in aqueous media under mild conditions, and indicate one route to electrification in the chemicals industry.

Methods

Materials. Potassium hexachloropalladate(IV) (99%), palladium(II) chloride (99%), palladium on carbon, palladium(II) oxide hydrate, palladium(II) oxide, gold(III) chloride solution (99.99% trace metals basis), sodium perchlorate (ACS reagent, ≥98.0%), palladium powder (≥99.9% trace metals basis), rhodium(III) chloride (98%), hydrazine hydrate, Nafion perfluorinated resin solution (5 wt.%), sulfuric acid, nitric acid and hydrochloric acid were purchased from Sigma-Aldrich. Palladium foil (99.9%) was purchased from Alfa Aesar. Nafion 117 proton exchange membrane was purchased from FuelCellStore. Ethylene (Grade 2.5, 99.5%) and argon (Grade 5.0, 99.999%) were purchased from Linde Gas. Carbon-13 ethylene (¹³C₂H₄, 99%) was purchased from Cambridge Isotope Laboratories. All the

chemicals were used without further purification. The mass flow controllers used in this work were purchased from Sierra Instruments. Deionized (DI; 18.2 MΩ) water was produced by a Millipore system and used for electrolyte preparation and the cleaning of experimental set-ups.

Preparation of catalysts. Palladium nanostructured dendritic (DNT) catalysts were fabricated using an electrochemical deposition technique in a solution of 2 mM K₂[PdCl₆] in 0.5 M H₂SO₄ in a glass beaker. A glassy carbon electrode (3 mm diameter) was used as the electrodeposition substrate, palladium foil was used as the counter electrode and Ag/AgCl (3.0 M KCl) was used as the reference electrode. A potential of -1.0 V vs Ag/AgCl was applied for a duration of 1,000 s in the electrodeposition process. The electrode was then rinsed with DI water and dried with a stream of nitrogen. Gold-doped Pd DNT catalysts were prepared by the addition of H[AuCl₄] to the palladium electrodeposition solution. H[AuCl₄] concentrations of 0.03, 0.08 and 0.2 mM were used to prepare catalysts with 1.8, 3.2 and 9.0 at.% gold, respectively. The same procedure was utilized with RhCl₃ to prepare rhodium-doped catalysts, with 0.03, 0.08 and 0.2 mM solutions used to prepare catalysts with 1.3, 2.5 and 5.4 at.% rhodium, respectively.

Palladium nanoparticles (Pd NPs) were synthesized by the reduction of PdCl₂ with N₂H₄ in aqueous solution. PdCl₂ (89 mg) was first dissolved in DI water (2.5 ml). N₂H₄ (1,000 mg) was dissolved in DI water (12.5 ml) and added dropwise to the PdCl₂ solution with stirring provided by a stirring plate and magnetic stirring bar. After the reaction was complete, the Pd NPs were washed with DI water and subjected to centrifugation. Finally, the Pd NPs were dried overnight in a vacuum oven.

Palladium on carbon, Pd powder, Pd NPs and PdO-H₂O were prepared for electrochemical testing by mixing the catalyst (10 mg) with methanol (1 ml) and Nafion perfluorinated resin solution (40 μl). The mixture was sonicated for 20 min to ensure uniformity. This solution (30 μl) was then drop-cast onto the glassy carbon electrode and left to dry for 30 min. Finally, the electrode was rinsed with DI water and dried with a stream of nitrogen.

Electrochemical measurements. All electrochemical measurements were carried out using an Autolab PGSTAT204 instrument in potentiostatic mode. In all experiments, a glass H-cell was used with an electrolyte volume of 25 ml in both the anode and cathode chambers. The H-cell was first cleaned in aqua regia before conducting the electrochemical measurements. Unless otherwise stated, 0.1 M NaClO₄ was used as the electrolyte, platinum foil was used as the cathode and a Nafion 117 membrane was used to separate the cathode and anode chambers. The flow rate of ethylene gas was kept constant at 30 standard cubic centimetres per minute (s.c.c.m.) and introduced into the cell using a mass flow controller. Ag/AgCl (3.0 M KCl) was utilized as the reference electrode. All current densities are reported on the basis of the geometric electrode area.

Products were quantified by ¹H NMR spectroscopy (600 MHz Agilent DD2 NMR spectrometer) using water suppression techniques. Dimethyl sulfoxide (DMSO) was used as the internal standard and D₂O as the lock solvent. For ¹³C NMR spectroscopy, proton decoupling techniques were employed to prevent ¹H protons from splitting the ¹³C nuclei, and samples were analysed continuously for 4 h to accumulate sufficient signal.

To calculate the FE toward all products, the following equation was used:

$$FE = NF \frac{n_{\text{product}}}{Q} \quad (3)$$

where N is the number of electron transfers required to generate the product from ethylene. N has a value of 2 for ethylene glycol, 4 for glycolaldehyde, 2 for oxirane, 2 for acetaldehyde and 4 for formic acid. n_{product} is the total amount of product produced (in moles). Q is the total charge passed through the electrochemical system during a bulk electrolysis measurement. F is the Faraday constant.

For the CO stripping studies, the electrolyte used was a CO-saturated 0.1 M HClO₄ solution (pH 1) with a potential of -0.2 V vs Ag/AgCl applied for 10 min. Immediately after this, the sparging gas was immediately changed from CO to N₂, with the same applied potential maintained for another 20 min, after which CO-stripping CV was performed. All the CVs were recorded at 20 mV s⁻¹ and the charge per area was taken to be 410 μC cm⁻².

Materials characterization. The surface morphology of Pd DNT was characterized by SEM using a Hitachi S-5200 microscope at a beam voltage of 15 kV. ICP-OES measurements were carried out on an Agilent 700 Series ICP-OES spectrometer operating in axial mode. Samples were prepared for ICP-OES analysis by dissolution in aqua regia solution. Operando X-ray absorption spectroscopy (XAS) measurements on Pd DNT were carried out at the 20BM beamline of the Advanced Photon Source (APS) located in the Argonne National Laboratory (Lemont, IL). XAS measurements for PdAu DNT were collected at the Advanced Light Source Beamline 10.3.2 located in the Lawrence Berkeley National Laboratory (Berkeley, CA). The Demeter system (v.0.9.26) was used to analyse and fit all the XAS data²⁷. XPS measurements were carried out on a ThermoFisher Scientific K-Alpha spectrometer with a monochromated Al-Kα X-ray source. TEM images were obtained on an FEI Titan 80-300 LB TEM, operated at 300 kV and equipped with a CEOS image corrector and a Gatan Tridiem energy filter. In situ Raman spectroscopy was performed using a Renishaw inVia Raman microscope with a water immersion objective using a 785 nm laser. A modified electrochemical cell was utilized with Ag/AgCl (3 M KCl) as the reference electrode and a coil of platinum wire as the counter electrode.

DFT calculations. In this work, all DFT calculations were performed using the Vienna Ab initio Simulation Package (VASP)^{28–31} with a periodic slab model using the projected augmented wave approach to describe the electron–ion interactions with a cut-off energy of 450 eV. The generalized gradient approximation with the Perdew–Burke–Ernzerhof exchange correlation functional³² was used and the effect of solvent was considered using the implicit solvent model implemented in VASPsol (ref. 33). To illustrate the long-range dispersion interactions between the adsorbates and catalysts, we employed the D3 correction method of Grimme et al.³⁴. Brillouin zone integration was accomplished using a 3 × 3 × 1 Monkhorst–Pack k -point mesh. The zero-point energy correction was included in all calculations and is given by:

$$E_{\text{ZPE}} = \sum_i \frac{h\nu_i}{2} \quad (4)$$

where h is Planck's constant and ν_i is the vibrational frequency i , which is calculated using the harmonic oscillators approximation. Four layers of PdO (100) surface were optimized, with the top two layers relaxed and the bottom two layers fixed. For simulations of the substitutional dopant, a palladium atom on either the subsurface or surface was replaced by a dopant atom. For DFT calculations, we adapted the grand canonical thermodynamics scheme to address the relative energetics based on the work by Nørskov et al.³⁵. Atomic coordinates of the optimized computational models are available on the Open Science Framework (<https://osf.io/rfmu9/>).

Data availability

The data that support the findings of this study are available from the corresponding author on reasonable request.

Received: 17 May 2019; Accepted: 24 October 2019;
Published online: 6 January 2020

References

1. *Annual Energy Review 2011* (U.S. Energy Information Administration, 2012).
2. *IPCC Climate Change 2014: Synthesis Report* (eds Core Writing Team, Pachauri, R. K. & Meyer L. A.) (IPCC, 2014).
3. Chu, S., Cui, Y. & Liu, N. The path towards sustainable energy. *Nat. Mater.* **16**, 16–22 (2017).
4. Davidson, D. J. Ennovating for a renewable energy transition. *Nat. Energy* **4**, 254–256 (2019).
5. Tackett, B. M., Gomez, E. & Chen, J. G. Net reduction of CO₂ via its thermocatalytic and electrocatalytic transformation reactions in standard and hybrid processes. *Nat. Catal.* **2**, 381–386 (2019).
6. Vogt, C., Monai, M., Kramer, G. J. & Weckhuysen, B. M. The renaissance of the Sabatier reaction and its applications on Earth and in space. *Nat. Catal.* **2**, 188–197 (2019).
7. De Luna, P. et al. What would it take for renewably powered electrosynthesis to displace petrochemical processes? *Science* **364**, eaav3506 (2019).
8. Orella, M. J., Román-Leshkov, Y. & Brushett, F. R. Emerging opportunities for electrochemical processing to enable sustainable chemical manufacturing. *Curr. Opin. Chem. Eng.* **20**, 159–167 (2018).
9. Sherbo, R. S., Delima, R. S., Chiykowski, V. A., MacLeod, B. P. & Berlinguette, C. P. Complete electron economy by pairing electrolysis with hydrogenation. *Nat. Catal.* **1**, 501–507 (2018).
10. Bondue, C. J., Calle-Vallejo, F., Figueiredo, M. C. & Koper, M. T. M. Structural principles to steer the selectivity of the electrocatalytic reduction of aliphatic ketones on platinum. *Nat. Catal.* **2**, 243–250 (2019).
11. Winiwarter, A. et al. Towards an atomistic understanding of electrocatalytic partial hydrocarbon oxidation: propene on palladium. *Energy Environ. Sci.* **12**, 1055–1067 (2019).
12. Huang, X., Zhang, Q., Lin, J., Harms, K. & Meggers, E. Electricity-driven asymmetric Lewis acid catalysis. *Nat. Catal.* **2**, 34–40 (2019).
13. Wang, A. & Zhang, T. One-pot conversion of cellulose to ethylene glycol with multifunctional tungsten-based catalysts. *Acc. Chem. Res.* **46**, 1377–1386 (2013).
14. Rebsdats, S. & Mayer, D. in *Ullmann's Encyclopedia of Industrial Chemistry* https://doi.org/10.1002/14356007.a10_101 (Wiley-VCH, 2000).
15. *Bio-Mono Ethylene Glycol (MEG) from Renewable Source An India Glycols Limited Case Study* International Council of Chemical Associations, 2017; https://www.icca-chem.org/wp-content/uploads/2017/12/ICCA_Infosheets_IGL.pdf
16. Verma, S., Lu, S. & Kenis, P. J. A. Co-electrolysis of CO₂ and glycerol as a pathway to carbon chemicals with improved technoeconomics due to low electricity consumption. *Nat. Energy* **4**, 466–474 (2019).
17. Jirkovský, J. S., Busch, M., Ahlberg, E., Panas, I. & Krtil, P. Switching on the electrocatalytic ethene epoxidation on nanocrystalline RuO₂. *J. Am. Chem. Soc.* **133**, 5882–5892 (2011).
18. Goodridge, F. & King, C. J. H. Oxidation of ethylene at a palladium electrode. *Trans. Faraday Soc.* **66**, 2889–2896 (1970).
19. Šebera, J., Hoffmannová, H., Krtil, P., Samec, Z. & Zálšíš, S. Electrochemical and density functional studies of the catalytic ethylene oxidation on nanostructured Au electrodes. *Catal. Today* **158**, 29–34 (2010).
20. Holbrook, L. L. & Wise, H. Electrooxidation of olefins at a silver electrode. *J. Catal.* **38**, 294–298 (1975).
21. Calle-Vallejo, F., Loffreda, D., Koper, M. T. M. & Sautet, P. Introducing structural sensitivity into adsorption–energy scaling relations by means of coordination numbers. *Nat. Chem.* **7**, 403–410 (2015).
22. Huang, Y.-F., Kooyman, P. J. & Koper, M. T. M. Intermediate stages of electrochemical oxidation of single-crystalline platinum revealed by in situ Raman spectroscopy. *Nat. Commun.* **7**, 12440 (2016).
23. D'Acapito, F., Davoli, I., Ghigna, P. & Mobilio, S. The refEXAFS station at the GILDA beamline (BM08) of ESRF. *J. Synchrotron Radiat.* **10**, 260–264 (2003).
24. Long, N. V. et al. The development of mixture, alloy, and core-shell nanocatalysts with nanomaterial supports for energy conversion in low-temperature fuel cells. *Nano Energy* **2**, 636–676 (2013).
25. Chen, C.-H. et al. Architecture of Pd–Au bimetallic nanoparticles in sodium bis(2-ethylhexyl)sulfosuccinate reverse micelles as investigated by X-ray absorption spectroscopy. *ACS Nano* **1**, 114–125 (2007).
26. Kaiser, J. et al. The structure of AuPd nanoalloys anchored on spherical polyelectrolyte brushes determined by X-ray absorption spectroscopy. *Faraday Discuss.* **162**, 45–55 (2013).
27. Ravel, B. & Newville, M. ATHENA, ARTEMIS, HEPHAESTUS: data analysis for X-ray absorption spectroscopy using IFFFIT. *J. Synch. Rad.* **12**, 537–541 (2005).
28. Kresse, G. & Furthmüller, J. Efficient iterative schemes for ab initio total-energy calculations using a plane-wave basis set. *Phys. Rev. B* **54**, 11169–11186 (1996).

29. Kresse, G. & Furthmüller, J. Efficiency of ab-initio total energy calculations for metals and semiconductors using a plane-wave basis set. *Comput. Mater. Sci.* **6**, 15–50 (1996).
30. Kresse, G. & Hafner, J. Ab initio molecular dynamics for liquid metals. *Phys. Rev. B* **47**, 558–561 (1993).
31. Kresse, G. & Hafner, J. Ab initio molecular-dynamics simulation of the liquid-metal–amorphous-semiconductor transition in germanium. *Phys. Rev. B* **49**, 14251–14269 (1994).
32. Perdew, J. P., Burke, K. & Ernzerhof, M. Generalized gradient approximation made simple. *Phys. Rev. Lett.* **77**, 3865–3868 (1996).
33. Mathew, K., Sundararaman, R., Letchworth-Weaver, K., Arias, T. A. & Hennig, R. G. Implicit solvation model for density-functional study of nanocrystal surfaces and reaction pathways. *J. Chem. Phys.* **140**, 084106 (2014).
34. Grimme, S., Antony, J., Ehrlich, S. & Krieg, H. A consistent and accurate *ab initio* parametrization of density functional dispersion correction (DFT-D) for the 94 elements H–Pu. *J. Chem. Phys.* **132**, 154104 (2010).
35. Nørskov, J. K. et al. Origin of the overpotential for oxygen reduction at a fuel-cell cathode. *J. Phys. Chem. B* **108**, 17886–17892 (2004).

Acknowledgements

This material is based upon work supported by the Ontario Research Fund Research Excellence Program, the Natural Sciences and Engineering Research Council (NSERC) of Canada and the CIFAR Bio-Inspired Solar Energy program. The authors thank Z. Finfrock and D. M. Meira for technical support at the 20BM beamline of the Advanced Photon Source (Lemont, IL). This research used resources of the Advanced Photon Source, an Office of Science User Facility operated for the US Department of Energy (DOE) Office of Science by Argonne National Laboratory and was supported by the US DOE under Contract No. DE-AC02-06CH11357 and the Canadian Light Source and its funding partners. We acknowledge S. Fakra and the use of Beamline 10.3.2 at the Advanced Light Source for the collection of XAS data. The authors thank C. Andrei of the Canadian Centre for Electron Microscopy (CCEM) for TEM analysis. D.S. acknowledges the NSERC for an E. W. R. Steacie Memorial Fellowship. J.L. acknowledges the Banting Postdoctoral Fellowships program. All DFT computations

were performed on the IBM BlueGene/Q supercomputer with support from the Southern Ontario Smart Computing Innovation Platform (SOSCIP) and Niagara supercomputer at the SciNet HPC Consortium. SOSCIP is funded by the Federal Economic Development Agency of Southern Ontario, the Province of Ontario, IBM Canada Ltd, Ontario Centres of Excellence, Mitacs and 15 Ontario academic member institutions. SciNet is funded by: the Canada Foundation for Innovation, the Government of Ontario, Ontario Research Fund—Research Excellence and the University of Toronto. We acknowledge the Ontario Centre for the Characterization of Advanced Materials (OCCAM) for characterization facilities.

Author contributions

E.H.S. supervised the project. Y.L. and E.H.S. conceived the idea and designed the experiments. Y.L. and J.E.H. carried out all the experimental work. Y.L. performed the DFT calculations. Z.W. supervised the DFT calculations. Y.L. and W.R.L. performed the TEA. M.L. carried out some of the TEM measurements. B.C. analysed the TEM results. Y.L. and D.H.N. carried out XAS measurements. Y.L. and J.L. analysed the XAS data. J.W. performed the XPS measurements. D.H.N. carried out PXRD measurements. Y.C.L. and Y.W. performed SEM measurements. C.-T.D., T.-T.Z., F.L., T.-K.S. and D.S. contributed to data analysis and manuscript editing. Y.L. and E.H.S. co-wrote the manuscript. All authors discussed the results and assisted during the manuscript preparation.

Competing interests

The authors declare no competing interests.

Additional information

Supplementary information is available for this paper at <https://doi.org/10.1038/s41929-019-0386-4>.

Correspondence and requests for materials should be addressed to E.H.S.

Reprints and permissions information is available at www.nature.com/reprints.

Publisher's note Springer Nature remains neutral with regard to jurisdictional claims in published maps and institutional affiliations.

© The Author(s), under exclusive licence to Springer Nature Limited 2020